REVIEW OF SCIENTIFIC INSTRUMENTS VOLUME 73, NUMBER 12 DECEMBER 2002

“Linearizing” an ion cyclotron resonance cell

S. E. Barlow[a)]
W.R. Wiley Environmental Molecular Sciences Laboratory, Pacific Northwest National Laboratory, P.O. Box 999 (K8-88), Richland, Washington 99352

Mark D. Tinkle
Dynamics Technology, Inc., 21311 Hawthorne Boulevard, Suite 300, Torrance, California 90503-5610

(Received 26 February 2002; accepted 4 September 2002)

We describe an ion cyclotron resonance (ICR) mass spectrometer that we have built. The design of the instrument was guided in large measure by theoretical consideration; in particular we wished to investigate the effects of improved electrostatic linearity on ICR performance. We found, for instance, that the trap's performance as a mass spectrometer is essentially independent of the trapping potential. By studying both cyclotron and magnetron modes we were able to characterize both the trap and the magnet. Further, we were able to separate effects of image charge from space charge; this gave us measurements of ion number and ion cloud shape. Finally, we show that the instrument readily provides accurate mass measurements with minimal calibration. © *2002 American Institute of Physics.* [DOI: 10.1063/1.1518787]

I. INTRODUCTION

Elementary discussions of ion cyclotron resonance (ICR) ion traps generally begin with a simplified form of the magnetic and electric fields. The magnetic field is taken to be uniform and oriented in the z direction.

$$\mathbf{B}=B_0\mathbf{z}, \tag{1}$$

and the electrostatic trapping potential is taken to be purely quadratic and cylindrically symmetric:

$$\Phi(x,y,z)=\frac{C_2V_T}{r_0^2}\left[-\frac{1}{2}(x^2+y^2)+z^2\right]. \tag{2}$$

Here, C_2 is a constant that depends on the shape of the electrodes and V_T is an applied potential. The “characteristic dimension” of the system is r_0; this term repeatedly appears in equations here. We use the trap's radius $r_0=2.000$ (± 0.0008) cm, as the characteristic dimension. Equations (1) and (2) are, of course, only approximations of the actual magnetic fields and electrostatic potentials. The quality of these approximations ranges from excellent in precision measurement instruments[1–4] to fair in most ICR cells,[5,6] to inappropriate for Malmberg–Penning trap.[7,8]

It may be possible to improve ICR mass spectrometers by more closely approaching the ideals embodied in Eqs. (1) and (2). Among the expected benefits are improved reproducibility of ICR frequencies, a wider useful range of trap potentials, and much simplified “tuning” of trapping and excitation parameters. Further, by reducing the confounding effects of external fields, unavoidable issues related to “space charge” can be studied cleanly. Such studies should lead to a better understanding of the true capabilities and limitations of the ICR as a mass spectrometer.

We have built an ICR with these issues in mind. The major thrust of the work described here is the characterization of the instrument itself from first principles rather than attempting to evaluate its performance as a mass spectrometer *per se*. Most of the measurements, protocols, and data treatments are quite different from those more commonly used for analytical work. Thus, comparison with other mass spectrometers is outside the scope of this article. (For an excellent review of analytical ICR mass spectroscopy see Marshall, Hendrickson, and Jackson[9] and references therein.) It is worth noting that Guan and Marshall[6] built an ICR cell with improved electrostatic characteristics presumably for the same reasons as we did. Unfortunately, their trap did not perform well for other reasons and the work was not pursued further.

Although this is primarily an “instrument” article, the design of the instrument was predicated on theoretical grounds. Thus, our presentation begins with the theoretical treatment and methods that led to the design and were later applied to the interpretation of results. Section II gives a brief review of the elementary treatment of the harmonic Penning trap and serves to establish our notation. In Sec. III we provide a more detailed discussion of the theory that underlies our final designs. Section III begins with the calculation of the trapping potential and an elementary model of the stored ion cloud. We also present models for the excitation and detection of magnetron and cyclotron motion. The last parts of Sec. III are devoted to low order perturbations and the effects of misalignment. The models we develop here make numerous predictions about ion cloud behaviors, however, we have only been able to carefully test a few of them. Section IV describes the instrument. Particular attention is paid to the trap itself and some of the more unusual features that we incorporated in the overall instrument design. Section V describes experiments that characterized the instrument. We found excellent agreement between the theo-

---

[a)] Author to whom correspondence should be addressed; electronic mail:se.barlow@pnl.gov

0034-6748/2002/73(12)/4185/16/$19.00

retical electrostatic parameters calculated in Sec. III and the measured ones. We were also able to separate ion space charge and image charge effects. Finally, we show a sample ICR spectrum and its analysis. We are routinely able to achieve mass accuracy better than 0.01 u with no special calibration.

Unless otherwise stated, all equations are written in SI units.

II. LINEAR EQUATIONS OF MOTION

When Eqs. (1) and (2) are at least approximately true, they may be inserted into the equations of motion for an ion of mass-to-charge ratio, m/q. The resulting second order linear differential equations can be readily solved. If we have $m/q>0$ and $B_0>0$, then stable trapping occurs when $V_T>0$. The (x,y) motion is cycloidal. We find

$$x(t)=r_m\cos(\omega_m t+\phi_m)+r_{\text{icr}}\cos(\omega_{\text{icr}}t+\phi_{\text{icr}}) \tag{3}$$

and

$$y(t)=-r_m\sin(\omega_m t+\phi_m)-r_{\text{icr}}\sin(\omega_{\text{icr}}t+\phi_{\text{icr}}), \tag{4}$$

where the subscript m refers to the low frequency ''magnetron'' or drift motion and the subscript icr refers to the high frequency ''ion cyclotron resonance'' motion. The constants in Eqs. (3) and (4) depend on the initial velocities and positions. Note that the *signs* of both of the coefficients change going from $x(t)$ to $y(t)$. This means that ion motion is clockwise for both magnetron and cyclotron motion. The ''sense'' of this motion plays a crucial role later in determining which harmonics of the motion can be observed. The frequencies in these equations are given by

$$\omega_{m0}=\frac{\Omega}{2}\left(1-\sqrt{1-4\frac{qC_2V_T}{mr_0^2\Omega^2}}\right) \tag{5}$$

and

$$\omega_{\text{icr}0}=\frac{\Omega}{2}\left(1+\sqrt{1-4\frac{qC_2V_T}{mr_0^2\Omega^2}}\right), \tag{6}$$

where $\Omega=qB_0/m$ is the cyclotron frequency. Equations (5) and (6) are related to each other by

$$\omega_{\text{icr}}=\Omega-\omega_m. \tag{7}$$

In the usual case for ICR, $4qC_2V_T/mr_0^2\Omega^2\ll 1$, so Eqs. (5) and (6) may be expanded to give

$$\omega_{m0}\approx\frac{C_2V_T}{B_0r_0^2} \tag{8}$$

and

$$\omega_{\text{icr}0}\approx\frac{qB_0}{m}-\frac{C_2V_T}{B_0r_0^2}. \tag{9}$$

In this approximation, the magnetron frequency is independent of both charge and mass, while the cyclotron frequency depends inversely on the mass-to-charge ratio. Generally, Eq. (9) is not good enough for accurate mass spectrometry. A better approach is to use the appropriate Taylor series expansion of Eq. (6).

Ions oscillate parallel to the magnetic field (the axial direction) in the harmonic electrostatic potential of Eq. (2). The solution of the equation of motion is simply

$$z(t)=a_z\cos(\omega_z t+\varphi). \tag{10}$$

Here, a_z is the amplitude of axial motion; φ is the phase; and ω_z is the axial frequency given by

$$\omega_{z0}=\sqrt{2\frac{qC_2V_T}{mr_0^2}}. \tag{11}$$

If an ion cloud consisting of a single mass-to-charge species is stored in the ICR, the center-of-mass motion is well described by Eqs. (5), (6), and (11) provided nonlinear effects due to the finite size of the ion cloud and image charge are sufficiently small. Said another way, the center-of-mass motions of the ion cloud are ''normal modes'' of the ion cloud/trap system and, therefore, decouple from those of the individual particles in the cloud.[10]

When the initial ion cloud consists of ions of various mass-to-charge ratios, as is commonly the case in chemical applications, analysis becomes much more complex.[11] However, the unavoidable effects of collisions between ion clouds of different mass-to-charge ratios can be masked or even enhanced by electric and magnetic field errors. This is because center-of-mass motion is no longer decoupled from the motion of the individual ions and energy can flow from the center-of-mass translation into thermal degrees of freedom. Thus, field errors can produce not only amplitude-dependent frequency shifts, but also enhanced damping. When these errors arise from the electrostatic potential, the effects are generally proportional to the applied trapping voltage–the lower the potential, the smaller the effect.

III. PERTURBATIONS

Sources of deviations from Eqs. (1) and (2) can be roughly divided into five categories. First are those due to the electrostatic design and these are the ones that we will devote the most attention to here. Second are ''time-dependent'' effects, by which we primarily mean noise. Noise can be the result of vibration, ground and shielding deficiencies and unstable electronics. Section IV, which discusses the instrument design and construction, includes outlines of the various efforts we made to minimize these difficulties. Third, ion–ion and ion–conductor interactions are unavoidable sources of perturbation. For most chemical applications, measurements involving a single ion are neither relevant nor practical, thus we must begin the task of trying to understand these effects from first principles. The fourth type of perturbation we consider is the alignment between the electric and magnetic fields. Our instrument was built with unusual alignment capabilities, which we discuss in Sec. IV and experimental results are given in Sec. V. The final source of inhomogeneity is the magnetic field. There is little that we can do about the magnetic fields with our current magnets except to avoid making them worse, as is discussed in Sec. IV. Our results in Sec. V show that we are very nearly at the point where room-temperature shim coils could be beneficial.

TABLE I. Solutions of cylindrically and azimuthally symmetric LaPlace's equation through eighth order.

Order	Coef.	Form
0	C_0	1
2	C_2/r_0^2	$-\frac{1}{2}r^2+z^2$
4	C_4/r_0^4	$\frac{3}{8}r^4-3r^2z^2+z^4$
6	C_6/r_0^6	$-\frac{5}{16}r^6+\frac{45}{8}r^4z^2-\frac{15}{2}r^2z^4+z^6$
8	C_8/r_0^8	$\frac{35}{128}r^8-\frac{35}{4}r^6z^2+\frac{105}{4}r^4z^4-14r^2z^6+z^8$

A. Approximate trapping potentials

In the limit of a uniform, properly aligned magnetic field, azimuthally symmetric electric fields and circular orbits, Eqs. (5) and (6), can be generalized to[12]

$$f_{\mathrm{icr}/m}=\frac{\Omega}{4\pi}\left[1\pm\sqrt{1-\frac{4}{m\Omega^2}\left.\frac{F(r)}{r}\right|_{r=r_{\mathrm{icr}/m}}}\right], \tag{12}$$

where the subscripts icr/m correspond to the ± on the right-hand side of Eq. (12) and are the ion cyclotron resonance and magnetron frequencies, respectively. The term $F(r)/r$ is the total radial force divided by r and evaluated at the cyclotron (or magnetron) radius of the ion cloud's center of mass. With the help of Table I, we may write

$$\frac{F(r)}{r}=-\frac{qC_2V_T}{r_0^2}-\frac{3qC_4V_T[r^2-2z^2]}{2r_0^4} -\frac{15qC_6V_T[r^4-6r^2z^2+4\sqrt{2}z^2]}{r_0^6}\cdots -\frac{q}{2}\frac{\partial\Phi(r,z)}{r\partial r}. \tag{13}$$

The first three terms on the right-hand side are due to the trap while the fourth term is the "image charge pseudopotential" addressed in the next subsection.[13] When terms in the trapping potential greater than C_2 are present, two undesirable effects arise. First, the mode frequencies depend on the excitation amplitude. Second, all of the motions are coupled. For instance, the center-of-mass cyclotron motion that is of greatest interest in ICR work is coupled to the individual ion's axial motion. This allows the coherent energy of the cyclotron excitation to "leak" into the ion cloud's thermal motion. The net effect is that the cyclotron motion is damped and the ion cloud warms up. Since typical excitation energies range from hundreds to thousands of eV, even a small energy transfer rate can be important. [Equation (13) also shows that the frequencies depend on the axial amplitude, z. In a recent article,[13] we related these terms to the axial extent of the ion cloud.]

Generally, the lowest order nonlinear terms create the most difficulty. Therefore, we seek a design that drives C_4 to zero. (Gabrielse, Haarsma, and Rolston[4] have presented a design that also sets C_6 to zero, but it is more complex than the one described here.) The design problem begins with a solution of Laplace's equation,

$$\nabla^2\Phi=0, \tag{14}$$

where the potential, Φ, is determined by the boundary conditions. Solutions to Eq. (14) are known for every orthonormal coordinate system that exists.[14] These solutions are generally in the form of infinite sums over products of special functions. For our purposes, the most useful of these series is the spherical harmonic expansion. This expansion uses Legendre polynomials and can be easily rewritten as a power series in x, y, z. Table I provides a list of the first five even terms of this power series for the case of a cylindrically symmetric system. (The major drawback of analytical techniques is that real electrodes never actually match the boundaries required by any coordinate system.[15])

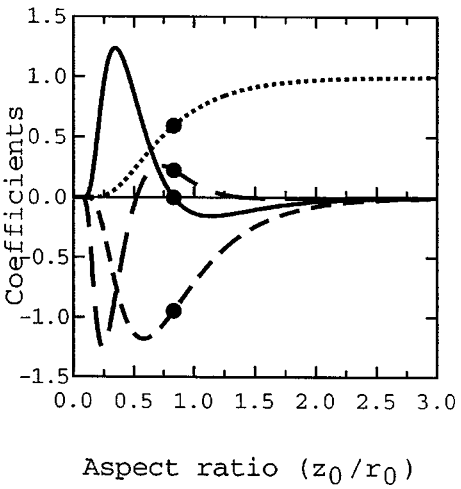

FIG. 1. Plot of C_n for $n=0(\cdots)$, 2(— — —), 4(—), 6(– –). Large dots are the theoretical values for the trap described here.

Since this was our first attempt to adapt this approach to ICR design, we decided to use a simple electrode structure based on disks for endcaps and a cylinder section for a "ring" electrode. The general solution of Laplace's equation in a cylindrical box is

$$\Phi=V\sum_{m=0}^{\infty}A(\alpha)\cos\left[\frac{(2m+1)\pi}{2z_0}z\right]I_0\left[\frac{(2m+1)\pi}{2z_0}r\right]. \tag{15}$$

Here, r_0 and z_0 are the trap's radius and half length, respectively, and $\alpha=z_0/r_0$ is the trap's aspect ratio. $I_0(x)$ is a Bessel function of the second kind of order zero. As Eq. (15) is written, the potential on the endcaps has been set to zero and the ring bias is V. The coefficients, A_m, are given by

$$A_m=4\frac{(-1)^m}{(2m+1)\pi I_0\left[\frac{(2m+1)\pi}{2\alpha}\right]}. \tag{16}$$

We now set $r=0$ in Eq. (15), expand the cosine in a Taylor series and rearrange the result to get series expressions for C_i. Figure 1 shows a plot of the first few terms as functions of α. We find that when $\alpha\approx0.831\,36$, $C_4\approx0$. This point is marked in Fig. 1 with heavy dots to indicate the values of the

TABLE II. Values of the coefficients of the spherical harmonic solutions of LaPlace's equation (Table I) for our trap. The "Nom." column is the result of the simple theory described in the text. Columns labeled "Tube" and "Slits" are estimated corrections to the nominal ones due to the access tubes through the endcaps and the slit ring, respectively. The determination of the values in the "Measured" column is described in Sec. V.

Order	Nom.	Tube	Slits	Total	Measured
C_0	0.594	<0.001	-0.003	0.591	a
C_2	-0.945	0.001	0.006	-0.938	-0.934 ± 0.001
C_4	0	0.003	0.002	0.005	0.00 ± 0.01[b]
C_6	0.224	0.006	-0.003	0.227	0.209 ± 0.003
C_8	-0.042	0.009	-0.002	-0.035	c

[a] Did not measure.
[b] Below measurable limit.
[c] Could not measure.

various C_i's for our particular trap. These numerical predictions are also given in the second column of Table II.

In addition to the values calculated for C_i by elementary means, Table II also reports our estimates of the effects of the ion entrance and exit apertures in the endcaps and the effects of slitting the ring electrode into eight pieces, as illustrated in Fig. 2. Distortions due to the 0.25 mm gap between the ring electrode and the endcaps as well as machining tolerances were also estimated, the former were found to be $<10^{-4}$ in all cases, while the latter were $<\pm10^{-3}$. The details of how these rough estimates were made need not concern us here. The last column of Table II gives the best estimate of these coefficients from the experimental data, see Sec. V. The three coefficients for which we have experimental data are in excellent agreement with our theoretical estimates.

B. Ion clouds and image charges

In order to be useful for chemical mass spectrometry, the ion trap must simultaneously store a fairly large number of ions. Further, these ions will commonly be divided into populations of different mass-to-charge ratios. These two facts introduce a host of additional complications and only a modest amount of theory exists to guide the ICR experimentalist.[11,12,16] In a broad sense, these issues fall within the purview of non-neutral plasma physics.[17,18] However, cyclotron motion has received relatively little attention from this community.

1. Elementary ion cloud model

Ions stored in a Penning trap all have the same charge sign, and because of the long-range nature of the Coulomb force, all of the charges are coupled to one degree or another with all of the others. For our purposes here we adopt the simple "uniform spheroid" model[16] to describe the electrostatics of the charged cloud and use standard formulations of ion–ion relaxation[19] to account for thermal and collisional processes.

In the uniform spheroidal or zero-temperature limit, an ion cloud is characterized by its axial length, $2z_p$, its diameter, $2r_p$, and its charge density, $q\rho$. In order for the charge density to be uniform, the axial space charge field must exactly cancel the axial trap field.[8] This condition is met when

$$\omega_z^2 = a(\chi)\omega_p^2, \tag{17}$$

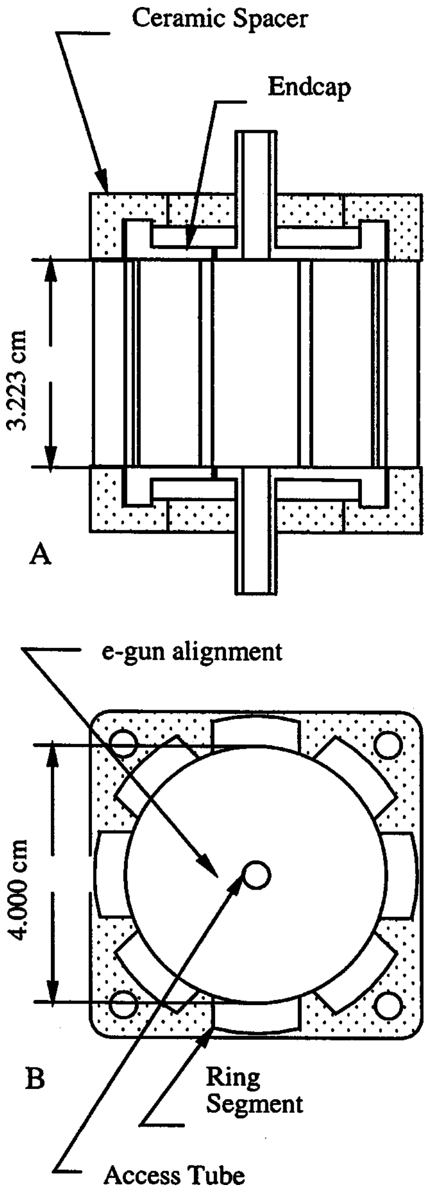

FIG. 2. Fourth order trap structure. (A) Cross section in the $x-z$ plane. (B) Cross section in the $x-y$ plane. Access hole allows on-axis introduction of ions and electrons from the external sources. "E-gun alignment" refers to 0.5 mm apertures in the endcaps that are used by the off-axis electron gun to align the trap with the magnetic field (see the text).

where $\chi = z_p / r_p$ is the ion cloud aspect ratio and ω_p is the plasma frequency:

$$\omega_p^2 = \frac{q^2 \rho}{\epsilon m}. \tag{18}$$

The function $a(\chi)$ is given by[20]

$$a(\chi) = Q_1^0 \left[\frac{\chi}{\sqrt{\chi^2 - 1}} \right] / (\chi^2 - 1). \tag{19}$$

Here, Q_l^m is the associated Legendre function of the second kind.[14] The electrostatic potential inside the ion cloud due to space charge can then be written

$$\Phi_{\mathrm{sc}}(r,z) = -\frac{q\rho}{4\pi\epsilon_0} \left\{ \left[\frac{1 - a(\chi)}{4} \right] r^2 + \frac{a(\chi)}{2} z^2 \right\}. \tag{20}$$

In this model, the axial motion of individual ions is governed by the thermal velocity, v_{th}. This oscillation is known as the ‘‘bounce frequency,’’ ω_b, and given by

$$\omega_b = \frac{\pi v_{th}}{z_p}. \tag{21}$$

Clearly, the bounce motion has a thermal distribution of frequencies.

The final piece of our simple ion cloud model is the ion–ion relaxation rate. Energy relaxation along the magnetic field and transverse to it is a complex subject.[12] In all cases, however, relaxation is proportional to the ion–ion collision rate

$$\nu_{i-i} = \frac{\rho (Zq)^4 \ln \Lambda}{2\pi\epsilon_0 m k_B T}, \tag{22}$$

where k_B is Boltzmann’s constant and $5 < \ln \Lambda < 20$ is the Coulomb logarithm.[19]

Transverse ion–ion collisional relaxation has an important consequence for ICR mass spectroscopy. In order to produce a mass spectrum, ions of each different mass-to-charge ratio must be coherently excited. If one attempts to add resonant energy too slowly, ion–ion collisions will simply dissipate it into thermal motion and no, or poor, ICR signals will be observed. Although this phenomenon is well known empirically among ICR practitioners, we are unaware that it has been studied quantitatively.

Our simple model makes a second prediction of relevance to ICR behavior. At temperatures commonly used in the laboratory, ions of different mass-to-charge ratios are distributed more or less uniformly in the equilibrium ion cloud.[21] Once the ions of differing masses are excited into their respective cyclotron modes, the axial space charge field no longer cancels the trapping field. The result is excess axial energy that ultimately must be converted to thermal motion of individual ions in their respective clouds. A minority species in the initial cloud can end up with so much excess energy that it cannot maintain coherence.[22]

A third prediction of the model concerns the cyclotron resonance response. Inside the quiescent, equilibrium cloud, the ion cyclotron frequencies are shifted by a combination of trapping and space charge fields.[16] However, the gyration frequencies of ion clouds of a single mass-to-charge ratio are determined by the trapping fields and their respective image charge forces, see below. In most cases, the cyclotron frequency in the equilibrium ion cloud will be at a lower frequency than that of the entire gyrating cloud. Thus, we might expect an asymmetric response to a chirp excitation depending on whether the frequency is swept up or down. In the case of a chirp with increasing frequency, the ions will tend to come into resonance sooner and remain in resonance longer than for a chirp from high to low. Further, lighter ions that are excited after the heavier ones have been ejected—thereby reducing the space charge and rotation frequency will be absorbing energy for a shorter time. Thus, we may expect a mass-dependent distribution of excitation radii. In the case of a sweep from high to low frequency, ions will tend to be in resonance for a shorter period of time. When the light ions are ejected, the cyclotron orbital frequency will increase for the remaining ions–in extremely pathological cases, this could cause a particular mass-to-charge ratio to never be resonantly excited. These should be subtle effects and can be completely masked by anharmonic effects.

Finally, the finite length of the ion cloud can give rise to additional frequency shifts of magnetron and cyclotron motion. This occurs because of the anharmonic terms of the trapping well and the image charge forces discussed below. This effect is also illustrated in Sec. V.

2. Image charge

In a recent publication,[13] we evaluated the effects of image charge on ion cloud motion in our trap. In particular, we showed for an ion cloud containing N ions of charge Zq and having a spheroidal shape that we could simply add a ‘‘pseudopotential’’ to the trap fields. For the particular geometry of our trap the ‘‘pseudopotential’’ has the form

$$\Phi_{\mathrm{image}} \approx -\frac{ZqN}{4\pi\epsilon_0 r_0} \left[\frac{0.753 r^2}{r_0^2} + \frac{0.776 z_p^2}{2 r_0^2} + \frac{1.124 r^4}{r_0^4} + \frac{0.916 r^2 z_p^2}{2 r_0^4} + \frac{1.167 z_p^4}{\sqrt{2} r_0^4} \right]. \tag{23}$$

Here, r is the amplitude of the cyclotron or magnetron orbit. The constants appearing in the numerators of each term are a result of the particular aspect ratio of our trap.[13] Equation (23) is correct to fourth order. We have no evidence that the higher order terms produce measurable effects in our system.

The use of z_p in Eq. (23) follows from our uniform spheroid model above. The ion cloud’s charge distribution allows us to define a ‘‘mean length’’ to the force acting on the ion cloud as it moves as a rigid body. This, in turn, leads to the substitution: $z^2 \rightarrow z_p^2/2$ and $z^4 \rightarrow z_p^4/\sqrt{2}$ in Eq. (13).[13]

3. Excitation and detection models

Figure 2(B) shows that the ring is divided into eight identical sectors with rather wide gaps between them. The sectors can be used to excite and detect magnetron and cyclotron motion. The gap width was chosen to facilitate the introduction of laser light across the trap in future work. The thickness of the electrodes serves two purposes, first it facili-

TABLE III. Values of $f(j)^{(\mathrm{ord})}$ for $j=0\ldots10$ and ord$=4$ and 8. The pattern displayed here continues beyond $j=10$. See the text for further discussion.

j	$f(j)^{(4)}$	$f(j)^{(8)}$
0	1	$\sqrt{2-\sqrt{2}}$
1	-1	$-\sqrt{2+\sqrt{2}}$
2	-1	$\sqrt{2+\sqrt{2}}$
3	1	$-\sqrt{2-\sqrt{2}}$
4	1	$\sqrt{2-\sqrt{2}}$
5	-1	$\sqrt{2+\sqrt{2}}$
6	-1	$-\sqrt{2+\sqrt{2}}$
7	1	$\sqrt{2-\sqrt{2}}$
8	1	$\sqrt{2-\sqrt{2}}$
9	-1	$-\sqrt{2+\sqrt{2}}$
10	-1	$\sqrt{2+\sqrt{2}}$

tates precise mounting of each sector and second it provides shielding from external perturbations through the slit gaps. The choice of eight rather than the more standard four or six sector designs was also made to facilitate future experiments. Finally, the slits' shape is intended to minimize interelectrode capacitance.

When these sectors are used to excite or detect ion motion, they act like antennas. We can calculate the force applied to stored ions by an excitation wave form and we can calculate the image current induced on these same electrodes by ion motion. For the work reported here, we selected a pair of opposing electrodes for excitation and connected the pair 90° away from this pair for our detectors. More recently, adjacent electrodes were connected to form quadrants. (Much more elaborate excitation/detection schemes are possible with this structure, but they have not been implemented.)

Analysis begins by writing down the "antenna" potential:

$$\Phi_{\mathrm{ant}}=\sum_{k=0}^{\infty}\sum_{j=0}^{\infty}A_{k,j}^{(\mathrm{ord})}I_{2j+1}\left(\frac{[2k+1]\pi}{2z_0}r\right)\times\sin([2j+1]\theta)\cos\left(\frac{[2k+1]\pi}{2z_0}z\right), \tag{24}$$

where we have added the subscript ant to Φ to distinguish it from the trapping potential. The coefficients $A_{k,j}^{(\mathrm{ord})}$ depend on the structure of the antenna. For the case where we use opposed quarter sections of the ring electrodes, $A_{k,j}^{(4)}$ is given by

$$A_{k,j}^{(4)}=16\sqrt{2}\,\frac{(-1)^k f(j)^{(4)}}{\pi^2(2j+1)(2k+1)I_{2j+1}\left(\frac{[2k+1]\pi}{2\alpha}\right)}, \tag{25}$$

while for the case of the eighth sections, $A_{k,j}^{(8)}$,

$$A_{k,j}^{(8)}=8\,\frac{(-1)^k f(j)^{(8)}}{\pi^2(2j+1)(2k+1)I_{2j+1}\left(\frac{[2k+1]\pi}{2\alpha}\right)}. \tag{26}$$

The $f(j)^{(\mathrm{ord})}$ are functions that have simple values and follow the patterns indicated in Table III. It is useful to expand Φ_{ant} in a spherical harmonic series, just as we did for the trapping potential. This allows us to identify the dominant terms and facilitates modeling calculations. Carrying out this expansion to third order we find for our trap that

$$\Phi_{\mathrm{ant}}^{(4)}\approx\{36.6-1.00(10)^5[x^2+z^2]+6.67(10)^4y^2\}y \tag{27}$$

and

$$\Phi_{\mathrm{ant}}^{(8)}\approx\{19.8-9.51(10)^4[x^2+z^2]+6.34(10)^4y^2\}y. \tag{28}$$

(Note that here the dimensions are in meters, but the relevant scales are in mm.) In comparing Eqs. (27) and (28) we see that the linear term is about twice as large for $\Phi_{\mathrm{ant}}^{(4)}$ as for $\Phi_{\mathrm{ant}}^{(8)}$ as we might guess from the geometry, however, the third order terms are about equal. In both cases, the linear term in y dominates near the center of the trap and deviates significantly at large distances. Relatively speaking, $\Phi_{\mathrm{ant}}^{(4)}$ is the more uniform of the two.

The force experienced by a ion due to an applied excitation voltage, $V(t)$, follows directly from Eq. (27) or (28):

$$\mathbf{F}(x,y,z,t)=-qZV(t)\boldsymbol{\nabla}\Phi_{\mathrm{ant}}(x,y,z), \tag{29}$$

where Z is the ion's charge state as before.

We can estimate the excitation amplitude for both r_m and r_{icr} by limiting our treatment to simple frequency chirp excitation and considering only the dipole term of the excitation field. By solving the inhomogeneous equations of motion—again limiting ourselves to the linear approximation—we find that when the chirp sweeps through the resonant frequency

$$r_{\mathrm{icr}/m}^{(4)}\approx2.28\frac{qZV_{p-p}}{m(\Omega-2\omega_m)\sqrt{\beta}}\approx3.23\frac{V_{p-p}}{B\sqrt{\beta}} \tag{30}$$

or

$$r_{\mathrm{icr}/m}^{(8)}\approx1.24\frac{qZV_{p-p}}{m(\Omega-2\omega_m)\sqrt{\beta}}\approx1.24\frac{V_{p-p}}{B\sqrt{\beta}}. \tag{31}$$

Here, V_{p-p} is the peak-to-peak amplitude of the excitation chirp; and β is the sweep rate of the chirp in hertz/s.

Ion motion causes the image charge on the electrodes to vary with time—an "image current." Somewhat surprisingly, the image current is far easier to evaluate than the image charge effects presented above. Schockley[23] showed that the image current in an electrode due to a particle of charge q at (x,y,z) and having a velocity $\mathbf{v}(x,y,z,t)$ was given by

$$I(t)=q\mathbf{v}(x,y,z,t)\cdot\boldsymbol{\nabla}\Phi_{\mathrm{ant}}(x,y,z), \tag{32}$$

where $\Phi_{\mathrm{ant}}(x,y,z)$ is identical to the potential we have just found. Our detectors have very high input impedance and low capacitance. Consequentially, our signals are proportional to the time-dependent portion of the image *charge*. This may be found by integrating Eq. (32) with respect to time:

$$\mathrm{Signal}(t)=\mathcal{A}(\omega)\int I(t)dt=\mathcal{A}(\omega)qZ\int\mathbf{v}(x,y,z,t)\cdot\boldsymbol{\nabla}\Phi_{\mathrm{ant}}(x,y,z)dt. \tag{33}$$

TABLE IV. Frequency and magnitudes of the Fourier components from ICR image charge detectors.

Frequency	Fourier coefficient for quarter sectors	Fourier coefficient for eighth sectors
f_m	$0.732\left[1+0.273\frac{2r_{\rm icr}^2+r_m^2}{r_0^2}\right]\frac{r_m}{r_0}$	$0.396\left[1+0.480\frac{2r_{\rm icr}^2+r_m^2}{r_0^2}\right]\frac{r_m}{r_0}$
$f_{\rm icr}$	$0.732\left[1+0.273\frac{r_{\rm icr}^2+2r_m^2}{r_0^2}\right]\frac{r_{\rm icr}}{r_0}$	$0.396\left[1+0.480\frac{r_{\rm icr}^2+2r_m^2}{r_0^2}\right]\frac{r_{\rm icr}}{r_0}$
$3f_m$	$0.333\frac{r_m^3}{r_0^3}$	$0.317\frac{r_m^3}{r_0^3}$
$3f_{\rm icr}$	$0.333\frac{r_{\rm icr}^3}{r_0^3}$	$0.317\frac{r_{\rm icr}^3}{r_0^3}$
$f_{\rm icr}+2\,f_m$	$1.000\frac{r_{\rm icr}r_m^2}{r_0^3}$	$0.951\frac{r_{\rm icr}r_m^2}{r_0^3}$
$f_{\rm icr}-2\,f_m$	$0.200\frac{r_{\rm icr}r_m^2}{r_0^3}$	$0.190\frac{r_{\rm icr}r_m^2}{r_0^3}$
$2\,f_{\rm icr}+f_m$	$1.000\frac{r_{\rm icr}^2r_m}{r_0^3}$	$0.951\frac{r_{\rm icr}^2r_m}{r_0^3}$
$2\,f_{\rm icr}-f_m$	$0.200\frac{r_{icr}^2r_m}{r_0^3}$	$0.190\frac{r_{\rm icr}^2r_m}{r_0^3}$

Here, $\mathcal{A}(\omega)$ is the transfer function of the detector circuit. Combining Eqs. (3), (4), and (30), or (31), we can find the lowest order expressions for the Fourier terms of the ICR signals. The results are summarized in Table IV. Clearly, when harmonics can be observed, the relative amplitudes at the various frequencies can be used to independently evaluate the amplitude of motion.[24]

Excitation and detection of ion motions has rightly received considerable attention from the ICR community over the years. Considerable effort has been devoted to understand the effects and to creating dipolar fields—much more so than we have here. One very effective design uses purely cylindrical electrodes that have been cut into sectors for use as excite/detect antennas. This topic is nicely presented in Marshall’s 1998 review referred to earlier.[9]

C. Very low order field perturbations

Before discussing the effects of misalignment, it is worthwhile to briefly review even simpler issues. In particular, we consider the effects of the lowest order deviations from Eq. (2). Equation (2) can be generalized to include a zero point offset, linear potential, and second order cross terms:

$$\Phi(x,y,z)=\Phi_0+\frac{C_x x+C_y y+C_z z}{r_0}+\frac{C_2 V_T}{r_0^2}\left[-\frac{1}{2}(x^2+y^2)+z^2\right]+\frac{C_{xy}xy+C_{xz}xz+C_{yz}yz}{r_0^2}. \qquad (34)$$

The first term is just a dc offset at the center of the trap. The only effect that this term has is on the kinetic energies of charged particles entering or leaving the trap. (See Laskin *et al.*[25] and Surko *et al.*[26] for interesting applications.) The next three terms correspond to uniform fields across the trap. Provided that they are sufficiently weak, these terms have the effect of shifting the origin or trap center. One example is the earth’s gravity. Normally, these terms are ‘‘harmless.’’[27] However, if the trap’s electric center is not located at the center of the magnetic field, problems associated with loading the trap from an external source can occur. This issue was addressed in some depth by Becker *et al.*[28]

The term $C_{xy}xy$ describes a linear electric field perpendicular to $\mathbf{B}$. It is easy to show that a rotation of the coordinate system about the $\mathbf{z}$ axis transforms $C_{xy}xy\rightarrow C_{\acute{x}\acute{y}}(\acute{x}^2-\acute{y}^2)$, which can then be added to the quadratic terms in the harmonic equations. The resulting equations of motion with this added term can still be solved analytically.[16] Magnetron and cyclotron orbits become elliptical and the corresponding frequencies are shifted, but no other essential differences from the cylindrically symmetric case exist.

The last two terms, $C_{xz}xz+C_{yz}yz$, are more serious. In a similar spirit to the previous case, we can find a rotation about the $\mathbf{z}$ axis that transforms one of the two terms to zero. Even with this transformation, motion parallel and perpendicular to the magnetic field becomes entangled. Terms of this sort can arise from angular misalignment of the electric and magnetic fields.

D. Alignment of the electric and magnetic fields

No matter how well constructed an ion trap is and no matter how uniform the magnetic field can be made, proper alignment is necessary. The location of the trap within the magnetic field is really a five-axis problem x, y, z, and θ, ϕ. That is, the center of the trap should to be located at the center of the magnetic field, where the field is most homogeneous, and the electric fields should ideally be aligned with the magnetic one. Becker *et al.*[28] have also considered this issue in some depth. Their experimental approach was closely related to the one described below.

1. Angular misalignment

In their paper on single ions in Penning traps, Brown and Gabrielse[29] treated the problem of a skewed trap explicitly. (They simultaneously also considered the effects of a small azimuthal eccentricity, which gives rise to a perturbation of the form x^2-y^2.) However, their analysis was restricted to small amplitude motion. We do not have that luxury in ICR applications, where the cyclotron orbits are typically and necessarily excited to large values. We show here that angular misalignment can set the upper mass limit for practical mass spectrometry.

Let us imagine an otherwise harmonic trap immersed in a uniform magnetic field, but skewed with respect to the field at an angle ϕ. We may without loss of generality set $\theta=0$. If we take the **z** axis to be parallel to **B**, then the electrostatic potential can be written

$$\Phi=\frac{C_2V_T}{r_0^2}\left[-\frac{1}{2}\{x^2+\cos^2(\phi)y^2\}+\{1-\tfrac{1}{2}\sin^2(\phi)\}z^2\right]. \tag{35}$$

The effects of skewing the trap are apparent from the equations of motion that follow from Eq. (35):

$$\frac{\partial^2 x}{\partial t^2}-\frac{qC_2V_T}{mr_0^2}x-\Omega\frac{\partial y}{\partial t}=0, \tag{36}$$

$$\frac{\partial^2 y}{\partial t^2}+\frac{qC_2V_T[1-3\cos(2\phi)]}{mr_0^2}y+\Omega\frac{\partial x}{\partial t}=3\frac{qC_2V_T[\sin(2\phi)]}{mr_0^2}z, \tag{37}$$

and

$$\frac{\partial^2 z}{\partial t^2}+\frac{qC_2V_T[1+3\cos(2\phi)]}{mr_0^2}z=3\frac{qC_2V_T[\sin(2\phi)]}{mr_0^2}y. \tag{38}$$

Here, we have written the $y\leftrightarrow z$ coupling terms as inhomogeneous forces. This is justified by the fact that normally $\omega_m\ll\omega_z\ll\omega_{\mathrm{icr}}$. In the case of the single ion, energy will move back and forth between axial and transverse motion. In extreme cases, the ICR signal will develop axial side bands and the axial signal will develop magnetron sidebands. For the ion cloud the effects are more profound. As energy moves back and forth between axial and transverse motions, ion–ion collisions will scatter some of the energy into internal thermal energy in the ion cloud and damp the coherent motion.

The magnitude of the damping due to skewness can be estimated. We imagine an ion cloud consisting of identical ions of mass $m=1.66\times10^{-27}$u and charge Zq. Our cloud has an ion number density of $\rho(\mathrm{M}^{-3})$, a center-of-mass temperature T(K), and a center-of-mass cyclotron radius r_{icr}. Further, we assume that we have neither center-of-mass magnetron or axial motion. In the limits of $\omega_{\mathrm{icr}}\approx\Omega\gg\omega_z$ and $\omega_z\gg\gamma_z$, where γ_z is the damping of the axial motion, Eq. (38) can be solved for the amplitude of the forced motion. We find

$$z(\phi)\approx3\frac{mC_2V_Tr_{\mathrm{icr}}}{qZr_0^2B_0^2}\sin(2\phi)\cos(\omega_{\mathrm{icr}}t). \tag{39}$$

Equation (39) can be interpreted as a nonresonant forcing of each ion individually. Summing over all of the ions in the cloud shows that the skewed field drives a coherent axial ''breathing'' motion. Such motion will be damped by ion–ion collisions at a rate ν_s, given approximately by[19]

$$\nu_s\approx6(10)^{-8}\frac{\rho Z^4}{\sqrt{u}T^{3/2}}, \tag{40}$$

which should be accurate to within an order of magnitude. The rate at which energy $\mathcal{E}_z$ (in eV) is lost from this mode is given by

$$\frac{\partial\mathcal{E}_z}{\partial t}\approx-\nu_s\frac{2ZC_2V_T}{r_0^2}\left[\frac{1}{\sin(\omega_{\mathrm{icr}}t)}\frac{\partial z(\phi,t)}{\partial t}\right]^2$$
$$\approx-2.8(10)^{-15}\left(\frac{C_2V_T}{r_0^2}\right)^2\frac{\rho Z^4r_{\mathrm{icr}}^2u^{1/2}}{B_0^2T^{3/2}}\sin^2(2\phi). \tag{41}$$

This energy loss will be mirrored by energy loss from the cyclotron motion:

$$\frac{\partial\mathcal{E}_c}{\partial t}\approx\frac{qZ^2B_0^2r_{\mathrm{icr}}}{m}\frac{\partial r_{\mathrm{icr}}}{\partial t}. \tag{42}$$

Equating Eqs. (41) and (42) and solving for $r_{\mathrm{icr}}(t)$, we get

$$r_{\mathrm{icr}}(t)\approx r_{\mathrm{icr}}(0)e^{-\gamma_ct},$$

where γ_c is the characteristic damping rate of cyclotron motion:

$$\gamma_c\approx2.9(10)^{-23}\left(\frac{C_2V_T}{r_0^2}\right)^2\frac{\rho Z^2u^{3/2}}{B_0^4T^{3/2}}\sin^2(2\phi). \tag{43}$$

The small leading coefficient makes the damping small for nominal ''normal'' values of the variables even when ϕ is large, e.g., 5°. However, Eq. (43) shows field misalignment can dominate damping for heavy, highly charged ions.[30]

The model embodied in Eq. (43) is new and has not been tested, however, this instrument has the capability to do so. In general, the study of damping and transport properties is of interest to the plasma physics community, see, e.g., Peurrung, Kouzes, and Barlow[12] or Dubin and O'Neil.[17] However, relaxation of the cyclotron motion in non-neutral systems is almost completely unstudied. Very recent experimental and theoretical work, see, e.g., Dubin.[31] indicates that collisional relaxation can proceed much more rapidly than was previously thought. The origin of the enhanced relaxation lies in the presence of nonlinear terms in the external fields, thus the predictions of our simple model may well represent a gross underestimate of the seriousness of the problem in ICR.

2. *x*,*y* misalignment

The major effect of miscentering in the magnetic field is observed when loading the trap from an external source. In a typical ICR instrument ions are produced in a source region at low magnetic field. (In our instrument the operator can choose an electron beam, a Cs^+ beam, or a beam from an electrospray source.) In a typical instrument, the "source" region is at a few gauss, while the field at trap is several tesla. Thus, ions (or electrons) from these external sources follow magnetic field lines that pass through the center of the magnetic field. If the trap is off center, the ion cloud will have a greater radius than otherwise. Further, beam–cloud interactions may induce magnetron motion.

E. The magnetic field

We have just treated the alignment of the electric and magnetic fields in some detail. So far, we have *assumed* that the magnetic field was completely uniform, see Eq. (1). In practice, we know that this cannot be true, however effects of an inhomogeneous magnetic field are seldom discussed topics in the ICR literature. Unfortunately, we have little control over the field quality. The superconducting magnet used for this work is described in Sec. IV below. We attempted to minimize field errors through careful materials selection and effects of vibration by mechanical means. The data presented in Sec. V indicate that we have reduced the electrostatic errors and uncertainties nearly to the point where we can test the manufacturer's field homogeneity specifications. It seems likely that future generations of ICR instruments will require room-temperature shims in much the same manner as nuclear magnetic resonance magnets do today.

IV. THE INSTRUMENT

In this section, we describe our instrument. We start with a description of the trap itself and closely related structures. Next, the bore tube, its mounting, and the trap gimbal is presented in some detail. In the last two parts of this section, we briefly touch on the electronics and vacuum cart design.

All of the experiments reported here were performed with a 7 T Oxford Instruments superconducting magnet. This magnet has a 6 in. horizontal bore and was installed and shimmed by Oxford technicians. We have attempted to minimize the perturbation of the magnetic field through careful selection of materials.

A. Design and construction of the fourth order trap electrodes

The overall description of the trap structure was presented earlier in connection with the electrostatic theory behind this instrument. Figure 2 shows two elevations of the trap structure. The agreement between our theoretical estimates of the trap's electrostatic parameters and our experimental measurements—described in the next section—indicates that the actual trap closely approaches the drawings.

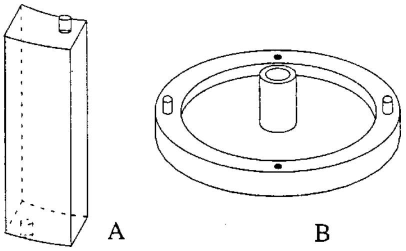

FIG. 3. (A) Segment of ring electrode. Note the locating pins on the top and bottom. (B) Sketch of an endcap electrode showing the central tube, mounting rim, locating pins.

The trap achieved the desired precision through a combination of high precision machining and design. The design includes a number of features that facilitated the trap's construction and allow it to be taken apart and reassembled with no loss of precision. At the heart of the design are two machinable ceramic insulators, shown on the top and bottom of Fig. 2(A), to which the locations of all of the trap's electrodes are referenced. Figure 3 contains perspective sketches of the electrodes. Each ceramic piece holds one of the endcap plates. Rims on the endcap plates locate them in z against a mating surface on the insulator. Further, each endcap has two beryllium–copper locating pins that fix their locations in x, y, and θ [Fig. 3(B)]. Each endcap is held in place by a pair of spring-loaded beryllium–copper screws. The ends of each ring segment butt against the ceramic pieces, as shown in Fig. 2(A). These segments are located by a pair of offset pins, as illustrated in Fig. 3(A). This arrangement of the pins ensures that each segment's location is completely determined, but never overconstrained. Finally, the entire trap structure is held together with four spring-loaded screws.

As illustrated in Fig. 3(B), each endcap has a central tube 4 mm in diameter and 10 mm long. These tubes allow the introduction of ions and electrons from the external sources while shielding the interior of the trap from external fields. Further, the large aspect ratio reduces the perturbation of the trapping fields due to their presence—see Table II. Each endcap electrode also has a 0.5 mm hole located 6 mm off the central axis. When the trap is properly assembled, these holes line up and allow us to use the off-axis electron gun for angular alignment of the trap.

The electrodes were fabricated from a single piece of 6061 aluminum. This alloy was chosen because of its ready availability, low magnetic susceptibility, and the ease with which it can be machined to high tolerances. Tolerances for critical dimensions were all set to ± 0.0003 in. $(\pm 8\mu)$, while the less critical dimensions were toleranced at the standard ± 0.005 in. $(\pm 125\mu)$. After machining and measuring, the electrodes were thoroughly degreased and sputter coated with gold. This coating prevents the formation of surface oxides that would compromise the electric field quality. However, since the gold was coated directly onto the aluminum, the trap structure must be kept below 150 °C to ensure continued adherence of the coating.

B. Ancillary electrodes and structures

In addition to the trap itself, the whole assembly has three ancillary parts. We have an "ion guide" located between the trap and external source region and two external

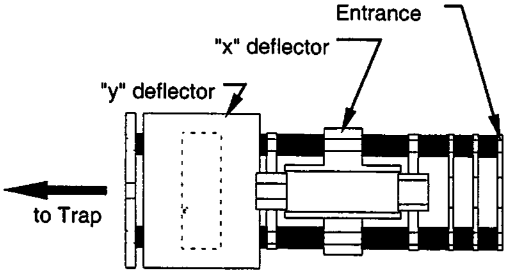

FIG. 4. Schematic drawing of the ion guide.

"ion gates" located just outside of the trap structure. Mounted off the ion gate electrodes is the off-axis electron gun and its collector.

1. Ion guide

The trap and its supporting electrodes are mounted on a gimballed flange. This means that alignment between the trap and an external source cannot be guaranteed. Thus, the trap is fitted with an external ion guide. This structure, illustrated in Fig. 4, consists of a series of gold-coated aluminum electrodes that allow an entering ion beam to be accelerated (or decelerated) parallel to the magnetic field and steered perpendicular to it. In the strong magnetic field near the trap, the deflectors produce an $\mathbf{E}\times\mathbf{B}$ drift. Normally, the drift velocity is much smaller than the acceleration produced by a simple nonmagnetized deflector, see, e.g., Jackson.[32] Thus, we found that we could readily steer an ion beam, but only very low energy electrons could be noticeably deflected.

The ion and electron sources originate in low magnetic fields. This means that the beams from these sources all end up on the magnet's axis. So long as the trap is within a few millimeters of the center and is not cocked more than a few degrees from the field, all external beams pass easily through the trap. Thus, the structure is not needed for routine applications. However, we were able to use the ion guide and the feet of the bore clamp to center the trap in the magnetic field to about 100μ. The explanation of this procedure is rather long and will, therefore, be deferred.

2. Ion gates

Just outside of each endcap electrode is an "ion gate." The gates are fabricated from 0.25 in. titanium plates and have 3 mm central apertures. The plates permit gated trapping without disturbing the fields inside the cell itself. Like so many of the original design features of this instrument, it has not yet been tested. However, the ion gates have proven valuable for a number of other applications.

The heftiness of the ion gates was specifically intended to allow them to support other structures. In particular, they support the off-axis electron gun assembly and its collector. We have also used the gate to support a collector to measure current from our external sources.

3. Off-axis electron gun

The off-axis electron gun is an alignment diagnostic as indicated earlier. The gun itself is housed in a precision machined ceramic block that fits in a slot on the ion gate located away from the external source region. The cathode is an 840μ tantalum disk emitter from Kimball Physics (Model ES-042), whose base was modified to fit in the holder. The anode is a titanium plate located 0.5 mm above the emitter disk and has a 1 mm aperture. The collector is mounted similarly to the gun on the ion gate located between the trap and the ion guide assembly.

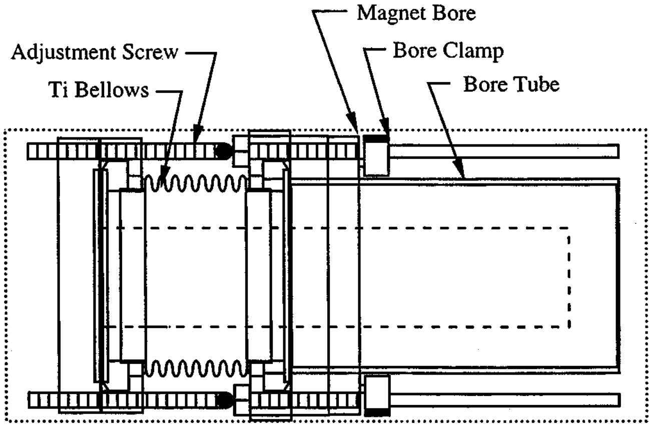

FIG. 5. Schematic of gimbal assembly and bore clamps.

C. Mounting flange

The ion trap with its ion gates, ion guide, and off-axis electron gun is mounted on a customized 6 in. knife edge flange made of titanium. The flange's diameter is somewhat less than the standard diameter and ports for 1.33 in. flanged feedthroughs have been machined on the outside face.

D. Bore tube assembly

Next to the trap and trap assembly, the "bore tube" and its associated parts received the most attention in our design. The assembly determines where the trap is located with respect to the magnetic field and provides both adjustment and vibrational isolation.

The bore tube nipple is fabricated from a 4 in. seamless titanium tube with welded knife-edge style flanges. As illustrated in Fig. 5, a formed titanium bellows is placed between the end of the bore tube nipple and the trap mounting flange. When the system is under vacuum, the bellows is prevented from collapsing by three 80 pitch brass screws. These screws allow angular adjustment of the trap assembly in the magnetic field.

Also shown schematically in Fig. 5 are two of the four "feet" that make up the bore clamp. These feet are mounted on a split brass ring that acts as a plate nut for mounting the bellows. Long actuator rods pass along the bore tube nipple and out the magnet's bore. When an actuator rod is rotated, a cam action moves its respective foot out to the bore. Each foot has a Viton pad to insure good contact with the bore tube wall and to provide additional vibrational damping. The feet not only clamp the assembly to the inside of the tube, but also allow the trap to be accurately centered in the magnet.

The final piece of the assembly is a Delrin flange that mounts onto the face of the magnet Dewar. This flange

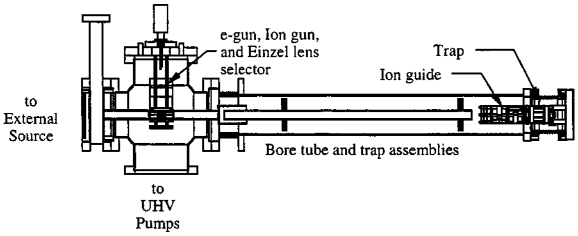

FIG. 6. Schematic sketch of the vacuum system.

snugly centers the bore tube in the magnet and holds the actuator rods in place. Radial screws in this flange prevent the actuator rods from rotating once the feet have been adjusted.

E. Vacuum system and support stand

As shown schematically in Fig. 6, the bore tube nipple is connected to the main vacuum system with a vibration isolator (NEC model VI-1). The vacuum system consists of two parts separated by a gate valve—the ultra-high-vacuum (UHV) section and a ‘‘source section.’’

The UHV system consists of an upper six-way cross and a lower three-way cross. The crosses are connected by an isolation gate valve and a second vibration isolator. The UHV pumps connect to the lower section and consist of a cryopump (Leybold RPK 900) and a titanium sublimation pump (Varian TSP filament cartridge). The base pressure of the UHV system is $1-2\times10^{-10}$ Torr.

The upper section to which the bore tube assembly is fixed contains an unusual structure. We have mounted a cesium ion source (Heat Wave Laboratories, model 1139), an external electron gun (Kimball Physics, model FRA-2X1-2 with EGPS-2X1 power supply) and an einzel lens on a translation stage. This allows us to switch among three ion sources without opening the vacuum system.

The vacuum system is mounted on a rather elaborate cart and movable rail system. This was originally intended to allow the system to be rapidly switched with a second system. Changing circumstances in the laboratory have obviated the importance of these features, however. The cart also has numerous features to minimize and damp vibrations. (Readers who are interested in this aspect should contact the authors.)

F. Electronics

Electronic support for the ion trap consists of three major subsystems. These are the source control, the trap control, and a computer data station. The computer data station was an Extrell (now Finnigan) system that has since been migrated to a MIDAS system.[33] Some of the data presented below were also taken with an HP spectrum analyzer (HP Model 4396B).

The source control subsystem contains the ion and electron source power supplies as well as the pump controllers and ion gauges. This subsystem is physically and electrically distinct from the trap controls. The separation of these two parts allows for a rationalization of the ground connections and power sources to minimize noise and cross talk among the various pieces of electronics.

The most refined piece of electronics is the trap control section. This section includes the trap voltage supply (Yokogawa model 7651 programmable dc source), a manually controlled dc bias supply for the ancillary electrode structures, and the excite/detect electronics.

At the heart of the detection system is a pair of very low noise preamplifiers. These amplifiers were fabricated in the EMSL Instrument Development Laboratory using a circuit designed by Jefferts and Walls.[34] Signals from the preamplifiers were differentially combined in an intermediate amplifier and then sent on to the data station for analysis. Excitation signals were generated by the data station which produces a 5 V peak-to-peak output. This output was coupled to a unity gain isolation amplifier and through a 5× step-up transformer to the excitation electrodes for the magnetron measurements. For cyclotron excitation, we used a rf amplifier (Amplifier research model 75A250) with the gain set to 58 dB.

V. CHARACTERIZING THE INSTRUMENT

We performed numerous tests and experiments to characterize the instrument and its performance. During the course of this work, we were able to verify many of the conjectures described in the theory section above. We also uncovered several unexpected phenomena, primarily having to do with magnetron motion. In this section, we describe these measurements and outline some of the procedures that we developed to characterize the trap’s parameters.

A. Noise

From the forgoing discussions, it is clear that we devoted considerable effort to minimize noise in the system. After the instrument was installed in the magnet, we ran noise tests to determine optimum shielding and grounding strategies. The simplicity of the system allowed us to find a suitable strategy rather quickly. Further, no noise attributable to vibration was ever detected.

The angular correction capability is by far the most elaborate of our independent adjustments. The diagnostic consists of the small off-axis electron gun mounted on one of the ion gates as described above. Since the electrons are so light, the path of the e-beam precisely marks the magnetic field. The gimbal assembly then allows us to adjust the angle of the trap with respect to the magnetic field. Actual adjustment consists of turning on the electron gun and monitoring the current at the collector on the opposite side of the trap.

B. Alignment

We found that the adjustment screws could be turned reproducibly through $\frac{1}{6}$ of a revolution. This corresponds to a displacement of 53μ or an angular resolution of about 1.7 min of arc. Figure 7 shows current to the diagnostic collector as a function of screw rotation for two nearly orthogonal screws. This means that the $\sin^2(2\phi)\leqslant10^{-6}$ in Eq. (43), and therefore effects due to angular misalignment are unlikely to

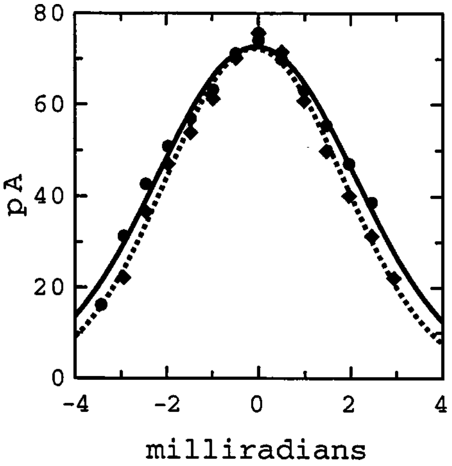

FIG. 7. Current vs angle for two nearly orthogonal adjustment screws. Lines through the data are Gaussian fits.

be measurable. Normally, the angular adjustment is performed in conjunction with the $x \leftrightarrow y$ alignment. Since the adjustments are not entirely orthogonal, we iterate the two procedures to fully align the trap.

C. Evaluating the trapping parameters

Following the model development of Secs. II and III, we rely primarily on two equations to evaluate the trap. These are the equation for ICR and magnetron frequencies and the one for excitation amplitude. Combining Eqs. (12), (13), and (20), and simplifying, we get

$$f_{\mathrm{icr}/m}=\frac{\Omega}{4\pi}\left\{1\pm\left[1-\frac{4}{m\Omega^2}\left(-\frac{qC_2V_T}{r_0^2}-\frac{15C_6V_T\{r^4-6r^2z_p^4+4\sqrt{2}z_p^4\}}{r_0^6}+\frac{q^2N}{\pi\epsilon_0}\left[\frac{0.188}{r_0^3}+\frac{0.562r^2+0.114z_p^2}{r_0^5}\right]\right)\right]^{1/2}\right\}. \tag{44}$$

Here, we have included the trap's field through sixth order and image charge effects through fourth order. We have set the C_4 term to zero, this will be justified by the data shown below. The second equation is the excitation amplitude, where we have inserted $B=7$ T in Eq. (31):

$$r_{\mathrm{icr}/m}^{(8)}\approx 0.177\frac{V_{\mathrm{p-p}}e^{dB/20}}{\sqrt{\alpha}}. \tag{45}$$

D. Evaluation of C_2, C_4, and C_6, and the offset potential

Figure 8 shows the results of measurements of the magnetron frequency with amplitude for both positive ions and electrons. Both charged clouds were produced by electron bombardment of the background gas with the trapping potential, V_T, set nominally at ±30 V. Figure 8 also shows the results of least-squares fits to a fourth order polynomial. Equation (45) was used to convert the excitation parameters to magnetron amplitudes.

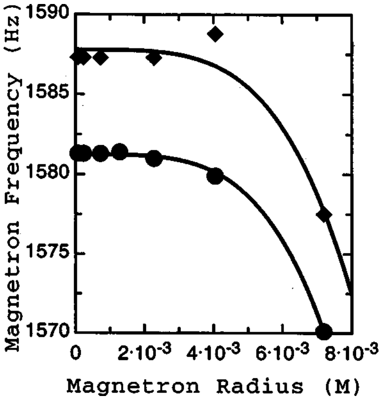

FIG. 8. Demonstration of lack of fourth order term in trapping potential. Diamonds are for a small electron cloud, while circles are from a small ion cloud.

With the help of Eq. (44), we can deduce a great deal about the trap from these data. The first point is that to within our ability to measure, $C_4=0$, as stated above. Second, since both the ion and electron clouds contained only a small number of charges, the contributions from image charge and ion cloud length can be ignored. We estimate the numbers to be <1000 based on electron impact cross sections. With these simplifications, Eq. (44) becomes

$$f_m\approx\frac{\Omega}{4\pi}\left(1-\sqrt{1-4\left[-\frac{C_2qV_T}{m\Omega^2r_0^2}-\frac{15C_6qVr^4}{m\Omega^2r_0^6}\right]}\right). \tag{46}$$

One can easily show from Eq. (46) that the magnetron frequency is nearly independent of mass for low mass ions; thus, we would expect that the frequencies in Fig. 8 should be identical within experimental error, but they clearly are not. Since the physical trap and magnetic field are unchanged between the measurement, the difference must lie in the applied trapping voltage V_T. If we write $V_Y=30+\delta V$ for the ions and $V_T=-30+\delta V$ for the electrons, and set $r=0$, we can ratio the two intercepts given in Table V. (Care must be taken with the signs of charge and frequency.) From the ratioing process we find

$$\delta V=0.054\pm 0.005\ \mathrm{V}. \tag{47}$$

We attribute this off-set voltage to an offset in the trap's bias supply of unknown origin. In all of our subsequent data analysis we incorporate this offset, but since its cause is unknown we assign a ±0.01 V uncertainty to the applied potential. This is one of the major sources of error in our analysis. We also find the ratio $B/C_2=7.545$; since we know from other sources that $B\approx 7.0469$ T, $|C_2|\approx 0.934$. With the inclusion of the voltage offset, Eq. (46) may be applied to the fits given in Table V to find C_6. These are the "experimental" values given in Table II.

TABLE V. Fits from data shown in Fig. 8.

Species	Intercept (Hz)	Coef.$\times r^4$ (Hz/M^4)
Electrons	1587.8 ± 0.5	$-3.7(10)^9\pm 5(10)^8$
Ions	1581.2 ± 0.1	$-4.1(10)^9\pm 6(10)^7$

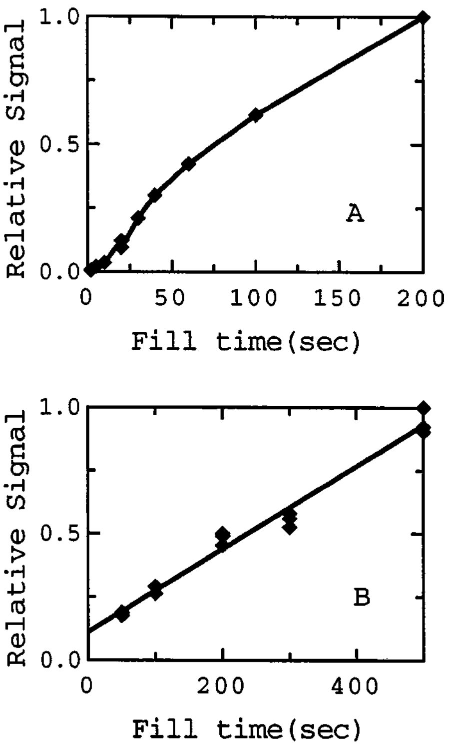

FIG. 9. Filling the trap from with an external beam source. (A) At early times, ion trapping is governed by ion–neutral scattering; estimated background pressure was 10^{-9} Torr. As ions begin to accumulate in the trap, ion–ion scattering dominates the loading process. At this point, the cloud expands axially and the number of stored ions increases exponentially. Eventually, the ion cloud reaches its maximum length and ions are only added by increasing the ion cloud's radius. Accumulation of ions then becomes approximately linear. (B) For the trap calibration measurements, filling times were 50, 100, 200, 300, and 500 s.

E. Magnetic field

By far the most important number is the magnetic field strength. The precision and accuracy of this measurement largely determines the accuracy with which other quantities can be ascertained. We made the determination of B with Cs^+ ions ($u = 132.904\,90$) from our external ion gun. The trapping voltage was set to 8 V and a steady beam of cesium ions (126 pA at 10 V) was introduced for various amounts of time. The ICR frequency and signal strength were then measured as a function of trapping potential using a weak chirp excitation. (The cyclotron radius was about 140μ.) Figure 9 shows ion signal strength with accumulation time. The measured ICR frequencies as functions of the applied trapping potential for each accumulation time were plotted and found to be linear. The frequency data were then fit to a straight line. The results of the fits are summarized in Table VI and plotted in Fig. 10.

TABLE VI. Measured ion cyclotron resonance frequencies for Cs^+ as functions of applied trapping potential and accumulation time.

Fill time	Intercept (Hz)	Slope (Hz/V)
50	814 215.5 ± 0.7	−52.95 ± 0.03
100	814 217.3 ± 0.7	−53.01 ± 0.03
200	814 210.0 ± 0.7	−53.05 ± 0.03
300	814 207.5 ± 0.7	−53.20 ± 0.03
500	814 201.0 ± 0.7	−53.39 ± 0.03

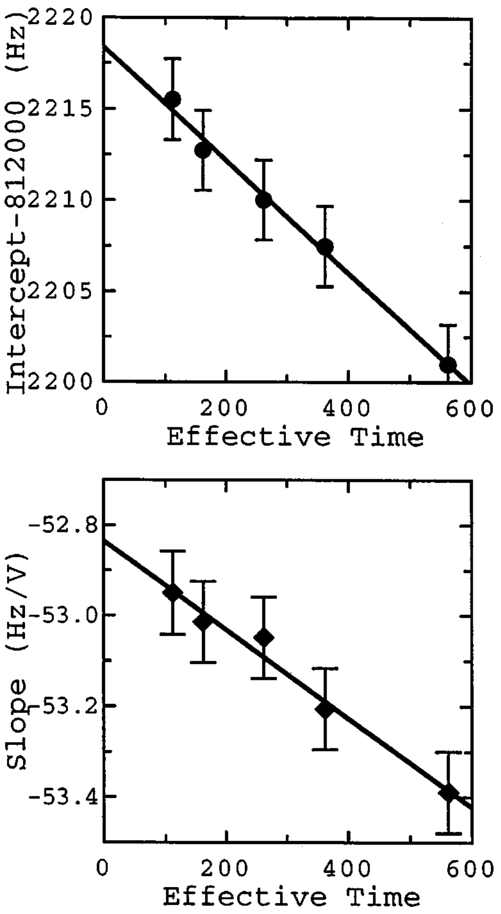

FIG. 10. Fitting of intercepts and slopes from Table VI vs effective accumulation time (see the text for explanation).

The line through the data in Fig. 9(B) is a simple linear fit given by

$$\text{Signal} = 0.32(\pm 0.01) + 0.0051(\pm 0.0001) \times t. \tag{48}$$

Comparing Figs. 9(A) and 9(B), the nonzero intercept is quite understandable. When the data of Table VI were plotted, we rescaled the time by adding 62 s and call it the "effective time." The lines through the data in Figs. 10(A) and 10(B) are also linear least-squares fits and are given, respectively, by

$$\text{Intercept(Hz)} = 814218.4(\pm 2.0) - 0.031(\pm 0.006) \times t \tag{49}$$

and

$$\text{Slope(Hz/V)} = -52.84(\pm 0.08) - 1.(10)^{-3}(\pm 2.(10)^{-4}) \times t. \tag{50}$$

We have no particularly strong theoretical reason to expect the results illustrated in Fig. 10, but we can exploit them to get a good estimate of the magnetic field and ion cloud parameters. From Eq. (49) we find the magnetic field in the trap:

$$B = 7.046\,935 \pm 0.000\,009 \text{ T}. \tag{51}$$

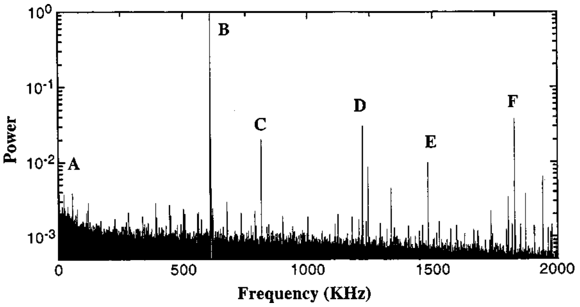

FIG. 11. Power spectrum of 12-Crown-4 ether ions produced by electron impact ionization followed by reactions with parent neutral molecules. Note that the vertical axis is logarithmic to accomidate the peaks and normalized to unity for the largest peak. Labels (A)–(F) refer to regions that are expanded in Fig. 12.

F. Ion cloud parameters

The linearity of the signal versus fill time illustrated in Fig. 9 is an important clue. Since ion trapping from the cesium beam is dominated by collisions between the trapped ions and the ions in the beam, the linear growth of the signal, and presumably the number of stored ions, implies that the collision rate is constant. That is, the product of the ion cloud's length, $2z_p$, and charge density $q\rho$ is constant. This implies that as ions are added to the cloud, it must expand radially. However, ion–neutral collisional transport is too slow to account for radial transport in the 7 T magnetic field and we must seek another process.

The experimental results in Eqs. (49) and (50) can be equated to the model in Eq. (44). Substituting in values for B, C_2, and C_6 that we have just found and making the assumption that the ion number, $N = n \times t$, $z_p(V_T, n, t)$ can be found. After simplification and elimination of the small terms we find

$$z_p \approx 3.4(10)^{-3} \times \left(\frac{[3.1(10)^{-5} n - 0.21]t - 0.71}{V_T} - 9.8(10)^{-3} t - 1 \right)^{1/4}. \tag{52}$$

Equation (52) should be approximately valid over the measured parameter space of $10 < V_T < 30$ V and $100 < t < 600$ s. Further, since z_p must be real and greater than zero, Eq. (52) places a definite lower bound on n, the rate of ion accumulation, of about 25 000/s.

The cesium ion gun has a diameter of 5 mm and was located in a 120 G field, thus at the trap the beam diameter would have been about 200μ. Further, the beam was centered in the trap to within 100μ, so the initial ion cloud radius would have been no more than 200μ. Finally, ion clouds tend to fill only about 10% of the electrostatic well,[35] which corresponds to a maximum half length of about 5.1 mm. Thus, the initial ion cloud volume was about 10^{-9} M^3. Since the aspect ratio, $\chi = z_p / r_p \approx 25$, is so large [see Eq. (17)], the electric field due to space charge will be mostly radial.[16] In this case the Brillouin density limit[18] is given by

$$\frac{\omega_p^2}{\Omega^2} = \frac{m\rho_{\max}}{\epsilon_0 B^2} \approx \frac{1}{2}. \tag{53}$$

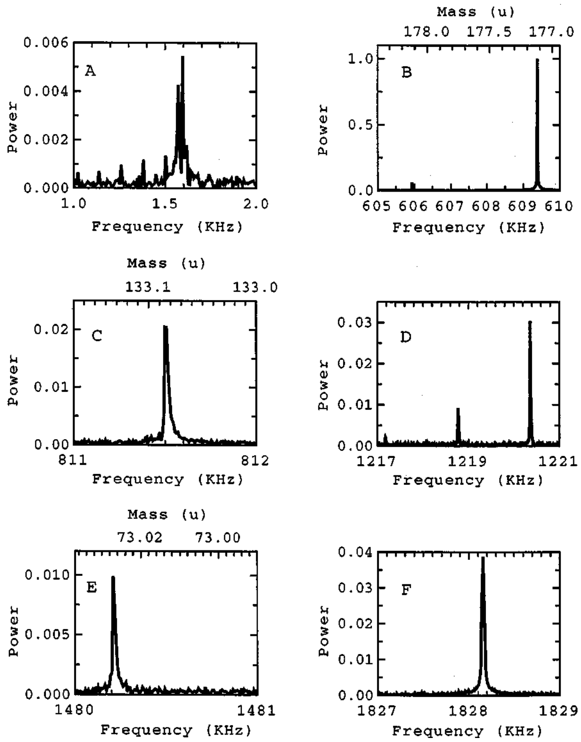

FIG. 12. Expanded regions of the power spectrum from Fig. 11 with linear vertical scales. (A) Magnetron signal; (B), (C), and (E) are mass peaks identified in Table VII, and hence, have mass scales; (D) and (F) are harmonics of the major peak and discussed in the text.

Here, we have ignored effects due to the trapping field and temperature, both of which will reduce $\rho_{\max}$ further. From our estimated initial cloud volume and ion accumulation rate, we conclude that the Brillouin density would be reached in about 40 s. It is interesting to note that even though the linear accumulation model does not apply for a short time, as shown in Fig. 9(A), the turnover from exponential to linear signal growth also occurs in this time frame. Once the Brillouin density is reached, ions are no longer radially confined by the magnetic field. As we continue to add ions, the ion cloud's radius will grow. Radial growth not only reduces density, but also changes the ion cloud's aspect ratio. In principle, the radial growth can be modeled with the help of Eq. (19), but doing so lies outside the scope of this article.

G. Sample mass spectrum

The focus of this article is primarily the quantitative characterization of our Penning trap ICR. To this end, we have employed a number of techniques not widely used by mass spectrometrists. However, it is also interesting to illustrate the instrument as a mass analyzer. A Fourier transform power spectrum is shown in Fig. 11. The ions were produced by electron bombardment of 12-Crown-4 ether in a 30 V well. The fragment ions were allowed to react with background gas for 10 s prior to excitation. The stored ion cloud was excited by a 178 $V_{\text{p–p}}$ chirp, that was swept at 50 MHz/s from 0.6 to 4 MHz. Subsequent analysis of the data was performed using a locally developed software package.[36] The labeled peaks in Fig. 11 are shown in expanded form in Fig. 12. Since only a few of these peaks correspond to actual ion

TABLE VII. Interpretation of spectra shown in Fig. 12. “ΔM” is defined as the difference between the calculated mass and the measured mass divided by the calculated value.

Fig. 12	Frequency (Hz)	Identification	Species	Calculated mass (u)	Measured mass (u)	ΔM
A	1 590	f_m	N/A			
B	605 934	$f_{\mathrm{icr}}(1)$	${}^{13}CC_7O_4H_{16}\cdot H^+$	178.114	178.122 $\pm$ 0.006	$-6(10)^{-5}$
B	609 383	$f_{\mathrm{icr}}(2)$	$C_8O_4H_{16}\cdot H^+$	177.111	177.116 $\pm$ 0.006	$-4(10)^{-5}$
C	811 501	$f_{\mathrm{icr}}(3)$	$C_6O_3H_{13}{}^+$	133.085	133.089 $\pm$ 0.004	$-3(10)^{-5}$
D	1 217 171	$2\,f_{\mathrm{icr}}(2)-f_m$	N/A			
D	1 218 765	$2\,f_{\mathrm{icr}}(2)$	N/A			
D	1 220 355	$2\,f_{\mathrm{icr}}(2)+f_m$	N/A			
E	1 480 209	$f_{\mathrm{icr}}(4)$	$C_3O_2H_5{}^+$	73.028	73.028 $\pm$ 0.002	$-8(10)^{-6}$
F	1 828 156	$3f_{\mathrm{icr}}(2)$	N/A			

masses, the spectra are shown as frequency data (see Table VII).

From the characteristics of the chirp excitation, Eq. (31) gives an estimate of the cyclotron radius: $r_{\mathrm{icr}} \approx 4.5$ mm. From the earlier analysis, we know that for $r_{m/\mathrm{icr}} < 4$ mm or so, the trap is essentially harmonic—see Fig. 8. So, we should expect anharmonicity to affect the frequency spectrum. Anharmonic effects should be obvious if we use Eq. (7) and use the measured value of the magnetron frequency—this model assumes that the system is purely linear. From Eq. (7) we find

$$m \simeq \frac{qB}{2\pi(f_{\mathrm{icr}}+f_m)}. \tag{54}$$

The specific frequencies corresponding to the various peaks and their assignments are listed in Table VII. Here, we used Eq. (51) for the magnetic field. The mass uncertainties arise from the ± 7 Hz uncertainty of the frequency measurements—due to the decay and the 9 μT uncertainty of the magnetic field. In most cases, the mass calculated from literature values falls just outside of the 1σ error bars and is most probably due to the anharmonicity just alluded to. The disparity between our values and those found in the literature could probably be reduced by using more standard ICR calibration techniques,[37] but the quality and quantity of these data are insufficient for the exercise to be meaningful.

By comparing the amplitudes of the peaks in Figs. 12(B) and 12(E), we can estimate the cyclotron radius from the formulas of Table IV. We find $r_{\mathrm{icr}} \approx 4.4$ mm, in excellent agreement with the value we calculated above. From the amplitude of the peak labeled $2\,f_{\mathrm{icr}}(2)-f_m$ in Table VII, we find that $r_m \approx 0.4$ mm. By contrast, the peak height associated with $2\,f_{\mathrm{icr}}(2)+f_m$ gives inconsistent values for both the cyclotron and magnetron amplitudes. Currently, we cannot explain this apparently anomalously large signal. Further, our signal model predicts no signal at $2\,f_{\mathrm{icr}}$; the presence of this peak is probably due to small differences between the amplifiers connected to the detection antennas.

ACKNOWLEDGMENTS

The research described in this article was performed at the W. R. Wiley Environmental Molecular Sciences Laboratory, a national scientific user facility sponsored by the Department of Energy's Office of Biological and Environmental Research and located at Pacific Northwest National Laboratory. Pacific Northwest National Laboratory is operated for the U.S. Department of Energy by Battelle under Contract DE-AC06-76RLO 1830. This work is supported in part by the U.S. Department of Energy Office of Basic Energy Sciences, Chemical Sciences Division. The authors would like to thank David Prior, Jim Follansbee, and Gordon Anderson for their support and assistance in the design and construction of the electronics. The authors also thank Dr. Anthony Peurrung, Dr. V. S. Rakova, and Dr. Julia Laskin for many valuable discussions. Finally, the authors wish to acknowledge Matthew Covert, their draftsman, and Lavon Clement, who built the support stand.

[1] F. L. Moore, L. S. Brown, D. L. Farnham, S. Jeon, P. B. Schwinberg, and R. S. Van Dyke, Jr., Phys. Rev. A **46**, 2653 (1992).

[2] E. A. Cornell, K. R. Boyce, D. Fygenson, and D. E. Pritchard, Phys. Rev. A **45**, 3049 (1992).

[3] T. P. Heavner, M. Zuo, P. Hayes, G. H. Dunn, and S. R. Jefferts, Phys. Scr. **T59**, 414 (1995).

[4] G. Gabrielse, L. Haarsma, and S. Rolston, Int. J. Mass Spectrom. Ion Processes **89**, 319 (1989).

[5] G. S. Jackson, J. D. Canterbury, S. Guan, and A. G. Marshall, J. Am. Soc. Mass Spectrom. **8**, 283 (1997).

[6] S. Guan and A. G. Marshall, Int. J. Mass Spectrom. Ion Processes **146**, 261 (1995).

[7] J. S. deGrassie and J. H. Malmberg, Phys. Fluids **23**, 63 (1980).

[8] S. A. Prasad and T. M. ONeil, Phys. Fluids **22**, 278 (1979).

[9] A. G. Marshall, C. L. Hendrickson, and G. S. Jackson, Mass Spectrom. Rev. **17**, 1 (1998).

[10] D. H. E. Dubin, Phys. Rev. Lett. **66**, 2076 (1991).

[11] A. J. Peurrung and R. T. Kouzes, Int. J. Mass Spectrom. Ion Processes **145**, 139 (1995).

[12] A. J. Peurrung, R. T. Kouzes, and S. E. Barlow, Int. J. Mass Spectrom. Ion Processes **157-158**, 39 (1996).

[13] M. D. Tinkle and S. E. Barlow, J. Appl. Phys. **90**, 1612 (2001).

[14] W. R. Smythe, *Static and Dynamic Electricity* (McGraw-Hill, New York, 1968).

[15] S. E. Barlow, A. E. Taylor, and K. Swanson, Int. J. Mass. Spectrom. **207**, 19 (2001).

[16] J. B. Jeffries, S. E. Barlow, and G. H. Dunn, Int. J. Mass Spectrom. Ion Processes **54**, 169 (1983).

[17] D. H. E. Dubin and T. M. ONeil, Rev. Mod. Phys. **71**, 87 (1999).

[18] R. C. Davidson, *Physics of Nonneutral Plasmas* (Addison-Wesley, Redwood City, CA, 1990).

[19] J. Huba, 1998 Revised NRL Plasma Formulary, Washington, DC (1998).

[20] J. J. Bollinger, D. J. Heinzen, F. L. Moore, W. M. Itano, D. J. Wineland, and D. H. E. Dubin, Phys. Rev. A **48**, 525 (1993).

[21] T. M. O'Neil, Phys. Fluids **24**, 1447 (1981).

[22] A. J. Peurrung and R. T. Kouzes, Phys. Rev. E **49**, 4362 (1994).

[23] W. Schockley, J. Appl. Phys. **9**, 635 (1938).

[24] E. N. Nikolaev, V. S. Rakova, and J. H. Futrell, Int. J. Mass Spectrom. Ion **158**, 215 (1996).

[25] J. Laskin, E. V. Denisov, A. K. Shukla, S. E. Barlow, and J. H. Futrell, Anal. Chem. **74**, 3255 (2002).

[26] C. M. Surko, R. G. Greaves, K. Iwata, and S. J. Gilbert, Nucl. Instrum. Methods Phys. Res. B **171**, 2 (2000).

[27] A. J. Peurrung and R. T. Kouzes, Int. J. Mass Spectrom. Ion Processes **139**, 39 (1994).

[28] S. Becker *et al.*, Rev. Sci. Instrum. **66**, 4902 (1995).

[29] L. S. Brown and G. Gabrielse, Rev. Mod. Phys. **58**, 233 (1986).

[30] As an example, our trap is currently operated in a 6 T magnetic field at 300 K. Assuming an ion density of $10^{12}/\mathrm{M}^3$, a trapping potential of 1 V, and angle of $1°$, we find that for ions of mass 10^4 u and $Z=10$ that the damping time is 450 s. For ions ten times heavier with three times the charge, the damping falls to about 0.7 s.

[31] D. H. E. Dubin, Phys. Plasmas **5**, 1688 (1998).

[32] J. D. Jackson, *Classical Electrodynamics* (Wiley, New York, 1975).

[33] M. W. Senko, J. D. Canterbury, S. Guan, and A. G. Marshall, Rapid Commun. Mass Spectrom. **10**, 1839 (1996).

[34] S. R. Jefferts and F. L. Walls, Rev. Sci. Instrum. **60**, 1194 (1989).

[35] S. E. Barlow, J. A. Luine, and G. H. Dunn, Int. J. Mass Spectrom. Ion Processes **74**, 97 (1986).

[36] G. A. Anderson, J. E. Bruce, and R. D. Smith, Technical Report, Pacific Northwest National Laboratory (unpublished), available at: http://www.emsl.pnl.gov/docs/msd/annual_report1999/1573b-4l.html

[37] S. D.-H. Shi J. J. Drader, M. A. Freitas, C. L. Hendrickson, and A. G. Marshall, Int. J. Mass. Spectrom. **195**, 591 (2000).